Comparative Studies of Reconstruction Algorithms for Sparse-View Photoacoustic Tomography

Xueyan Liu ⓘ, *Member, IEEE*, Shuo Dai ⓘ, Xin Wang ⓘ, and Mengyu Wang ⓘ

Abstract—Inverse source reconstruction is one of the most challenging problems in photoacoustic tomography (PAT) due to its ill-posed nature. Despite the extensive work done by researchers on this problem, there is currently no universally accepted solution. Regularization methods assume a significant role in the sparse-view PAT inverse problem. This study compares six inverse source reconstruction methods based on Lp ($0 \leq p \leq 2$) regularization and investigates the effects of signal sampling quantity, measurement noise, and sparsity on the performance of the reconstruction algorithms through a series of numerical simulations. The experimental results indicate that the average peak signal-to-noise ratio of the iterative hard threshold (IHT) method is twice that of the Tikhonov method and 3 dB higher than that of the L1magic method. The average running time of the IHT method is half that of the Tikhonov method and one-seventh of the L1magic method. To further assess the performance of these six reconstruction methods, we conducted agar phantom experiments to examine their ability to resolve details. The aim is to provide valuable guidance for the development and application of algorithms in relevant fields.

Index Terms—Photoacoustic tomography, medical imaging, sparse-view acquisition, image reconstruction, hard thresholding algorithms.

I. INTRODUCTION

AS A promising non-invasive biomedical imaging modality, photoacoustic tomography (PAT) has gained rapid development in the last two decades [1]. PAT utilizes pulsed laser light to excite tissues, leading to the generation of ultrasonic waves through the photoacoustic effect [2]. By detecting and analyzing these waves, PAT can reconstruct high-resolution images of tissue optical absorption distribution [3]. Unlike pure optical imaging techniques, PAT overcomes the limitations of imaging depth by utilizing the excellent tissue penetration capability of ultrasound waves. Its ability to provide high-resolution images, functional information, and molecular imaging capabilities makes PAT a valuable tool for detecting diseases [4], [5]

and studying biological tissues [6], [7]. However, in practical applications, obtaining complete photoacoustic signals is often challenging due to limitations such as imaging depth, shielding effect, beam shape, and scattering [8], [9]. To address these challenges, sparse sampling technology provides an effective solution to improve imaging efficiency. Additionally, improving imaging hardware, optimizing reconstruction algorithms, and developing new methods also contribute to enhancing the performance of PAT [10], [11]. Various sparse-view PAT techniques, such as compressed sensing (CS) and deep learning (DL) based reconstruction methods have been developed to tackle these challenges.

In many imaging modalities, image reconstruction from incomplete data can be mathematically formulated as an underdetermined linear system. In order to obtain the accurate solution of the problem, additional assumptions or constraints must be incorporated into the reconstruction algorithm. CS theory has been widely used in PAT to mitigate the underdetermined and ill-posed problem caused by incomplete and sparse measurements. In PAT imaging, the image can be constrained to have a sparse representation in a specific transform domain, such as wavelet or total variation [12]. For example, L_1-norm regularization promotes the sparsity of the images and suppresses irrelevant or low-intensity features in the images, making the solution more efficient and accurate [13], [14], [15]. Total variation (TV) regularization maintains the sharpness of edges in the images by emphasizing the gradient information [16], [17]. Researchers have also sought to combine different types of regularization to take advantage of their strengths [18], [19], [20]. Regularization methods that incorporate a priori information are able to improve image quality and reduce artifacts in sparse-view PAT. However, they suffer from computational burdens due to the large size of the imaging model matrix.

In recent years, various deep learning (DL) approaches have shown significant potential in medical image reconstruction, including convolutional neural networks [21], [22], recurrent neural networks [23] and generative adversarial networks [24]. There are several DL architectures designed to learn end-to-end mapping, directly reconstructing the PAT image from raw signals [25], [26], [27]. While DL methods offer promising results for PAT image reconstruction and processing, there are still challenges that need to be addressed. These challenges include the limited availability of labeled data for training, the incorporation of prior knowledge into DL models, and the robustness of trained networks when dealing with different test data [28]. Previous studies indicated that DL is faster than CS-based methods for

image reconstruction, as it can leverage pre-trained models and reduce the optimization process. However, CS has performs better in preserving weak signals with a lower sampling rate since it exploits the sparsity of the data. Therefore, choosing between CS and DL for image reconstruction depends on the specific application and the characteristics of the data being processed [29].

So far, L_1-norm and TV regularization have been widely employed as regularization techniques in sparse-view PAT image reconstruction [12], [17]. Furthermore, alternative regularization approaches, including wavelet-based and L_0-norm regularization, can also be employed in the context of sparse-view PAT. By decomposing the image into different frequency bands, the wavelet transform can help to identify the most relevant features of the image and reduce the impact of noise and artefacts [30]. L_0-norm regularization enforces hard sparsity by setting all but the k largest coefficients to zero and promotes exact sparsity in a signal or image [31], [32]. Recently, the iterative hard thresholding (IHT) algorithm has developed to solve the problems related to L_0-norm regularization optimization [33] and has been successfully applied in many areas of biomedical imaging. For example, Wang et al. have used an adaptive Newton IHT to improve the performance of bioluminescence tomography [34]. Yuan et al. have applied the IHT algorithm to solve the inverse problem of Fluorescence molecular tomography [35]. By combining the K-wave toolbox with the hard thresholding pursuit method, it is possible to obtain a fast and high-quality sparse reconstruction of photoacoustic images [36]. The above articles have demonstrated that the hard thresholding algorithm and its variants can generate sparse models with high prediction accuracy for various applications.

In this work, the IHT algorithm and its three variants are used to optimize the sparse-view PAT image reconstruction on both simulation and agar phantom data [37], [38], [39]. They are also compared with the conventional Tikhonov regularization and L1magic. The structure of the paper is arranged as follows. The second section introduces the photoacoustic theory and the CS-based reconstruction methods. The third part describes the process and results of both numerical simulation and agar phantom. Conclusions are made in Section IV.

II. METHOD

A. Photoacoustic Theory

The photoacoustic wave equation is a key equation in photoacoustic theory that links the photoacoustic signal $p(r, t)$ at position r and time t to the absorbed energy density $A(r)$ within a material [3]. It can be mathematically described as follows:

$$\left(\nabla^2 - \frac{1}{c^2}\frac{\partial^2}{\partial t^2}\right)p(r,t) = -\frac{\beta}{C_p}A(r)\frac{dI(t)}{dt}, \quad (1)$$

where ∇^2 is the 3D Laplacian operator, $I(t)$ is the temporal profile of illuminating pulse that can be represented by the Dirac delta function. The quantities c, C_p, β denote the speed of sound in the medium, heat capacity, and isobaric volume expansion coefficient respectively. When the object possesses homogeneous acoustic properties, the received ultrasonic wave

$p(r_0, t)$ at the ultrasound detector position can be expressed as

$$p(r_0,t) = \frac{\beta}{4\pi C_p}\iiint \frac{A(r)}{|r_0 - r|}\frac{dI(t-|r_0-r|/c)}{dt}d^3r. \quad (2)$$

By taking the Fourier transform on the variable $\bar{t} = ct$, (2) can be rewritten in the Fourier domain as follow

$$\bar{p}(r_0,k) = \frac{-i\omega\beta}{4\pi C_p}\iiint A(r)\frac{\exp(ik|r_0-r|)}{|r_0-r|}d^3r. \quad (3)$$

Where $k = 2\pi f/c$ with frequency f. In the inverse problem of PAT, the goal is to estimate the $A(r)$ from the measured data $\bar{p}(r_0, k)$. In practical experiments, the frequency-domain data can be obtained by applying the Fourier transform to the time-domain signal. More compactly

$$Y = KX + e, \quad (4)$$

where $Y = (y_1, y_2, \cdots y_M)^T$ represents the frequency domain data and M is the signal number, $X = (x_1, x_2, \cdots x_N)^T$ is a vector that represents the absorbed energy density $A(r)$ and N denotes the pixel number, e is the measurement noise. K is the forward operator with the size of $M \times N$ that we discretize

$$K_{(m,n)(i,j)} = ick_n\frac{e^{-ik_n|r_m-r_{ij}|}}{|r_m - r_{ij}|}g_n, m$$
$$= 1, 2, \cdots, p, n = 1, 2, \cdots, q, \quad (5)$$

where m and n are the serial number of the detector location and frequency, i and j are the Cartesian coordinates.

B. CS-Based Iterative Reconstruction Algorithm

Mathematically, sparse-view and limited-angle PAT image reconstruction is an ill-posed inverse source problem. This is a very challenging problem in practical applications. In general, classical analytical algorithm can obtain good image quality with complete data. However, in the case of insufficient data, the quality of the reconstructed image is seriously degraded, and regularization methods are needed to improve the quality of the PAT image. The Tikhonov regularization method based on L_2 norm provides a powerful and general framework for solving ill-posed inverse problems. Its simplicity, the effectiveness of noise reduction and enhanced stability, and the theoretical basis contribute to its wide application in various fields, including image reconstruction [40], signal processing, and scientific computing. The Tikhonov regularization method can be expressed as follows:

$$\min_X \frac{1}{2}\|Y - KX\|_2^2 + \lambda\|X\|_2^2, \quad (6)$$

where λ is a regularization parameter. Equation (6) can be effectively solved through the LSQR algorithm [41]. However, the stronger smoothening effect of the Tiknonov regularization tends to blur the edges and small details in the image, which can lead to the loss of fine structures.

The CS theory suggests that if the image is sparse under an appropriate basis, it can be accurately reconstructed from a small amount of measurement data. Fortunately, most medical images exhibit a high degree of sparsity under a suitable transform

basis $\Psi : X = \Psi\theta$, where $\theta \in R^N$ is a vector containing the transform coefficients. It has been proved that the wavelet basis can provide a better CS matrix [12]. Four-level discrete wavelet transform was used the transform basis as in this paper. By denoting $\mathbf{A} = \mathbf{K}\Psi$, the sparsest solution can be found by solving the following L_0-norm regularized optimization problem

$$\min_{\theta} \frac{1}{2} \|Y - A\theta\|_2^2 + \lambda\|\theta\|_0. \qquad (7)$$

where λ is a regularization parameter to balance the data fidelity term and sparsity. However, the nonconvex L_0-norm minimization problem is combinatorial and difficult to solve. It has been confirmed in the literature that L_1-norm is a good approximation of L_0-norm, so L_1-norm regularization is often adopted instead in CS image reconstruction, which can be denoted as

$$\min_{\theta} \frac{1}{2} \|Y - A\theta\|_2^2 + \lambda\|\theta\|_1. \qquad (8)$$

Currently, three commonly used menthods implemented in Matlab (L1magic [12], SPGL1 [13], YALL1 [9]) have been used to reconstruct PAT image and achieved good results. However, L_1-norm regularization usually has some serious flaws, such as over-sparseness.

The iterative hard thresholding (IHT) algorithm is one of the important methods for solving the non-convex optimization problems based on the L_0-norm, and it is widely used in the fields of sparse estimation and CS image reconstruction [34], [35], [36]. The standard IHT algorithm initially proposed by Thomas Blumensath is used to solve the following sparsity-constrained optimization

$$\min_{\theta} \frac{1}{2} \|Y - A\theta\|_2^2 \, s.t. \|\theta\|_0 < s, \qquad (9)$$

where s is the sparse level and assumes that it is known. By starting with $X^0 = 0$ and using a very simple iterative procedure

$$X^{n+1} = H_s\left(X^n + A^T(y - AX^n)\right), \qquad (10)$$

where H_s is a nonlinear operator, which preserves only the s largest magnitude. The IHT method converges to a local minimum of the sparsity-constrained optimization problem in (9). There exist some improved algorithms based on the IHT to solve (9), such as improved iterative hard thresholding (IITH) algorithm [37], Newton hard-thresholding pursuit (NHTP) [38], conjugate gradient iterative hard Thresholding (CGIHT) [39], for solving the nonnegative sparsity optimization, and so on.

C. The Evaluation Factors

In order to evaluate the efficiency and accuracy of the PAT image reconstruction algorithm, several quantization parameters were utilized as quantitative factors. These parameters include the running time, peak signal-to-noise ratio (PSNR), relative error (RE), and structural similarity (SSIM). The running time assesses the efficiency of the reconstruction algorithm, while the PSNR estimates the quality of reconstruction. The RE measures the disparity between the reconstructed image and the ground truth image. Furthermore, this work utilizes SSIM as an image quality assessment metric to measure the similarity between the reconstructed image and the ground truth image. The SSIM is widely recognized and employed for evaluating image performance. The PSNR is defined as

$$PSNR\left(\widehat{X}\right) = 10 * \log_{10} \frac{N * \max(X)}{\left\|\widehat{X} - X\right\|_2^2}, \qquad (11)$$

where $\widehat{X}$ is the reconstructed image and $\max(X)$ means the maximum pixel value, which is 1 in the numerical experiments. The RE can be defined by

$$\mathrm{RE}\left(\widehat{X}\right) = \frac{\left\|\widehat{X} - X\right\|_2}{\|X\|_2} \times 100\%, \qquad (12)$$

The SSIM measures the luminance, contrast, and structure of an image, and can be mathematically represented as:

$$SSIM = \frac{\left(2\mu_X\mu_{\widehat{X}} + C1\right)\left(2\sigma_{X\widehat{X}} + C2\right)}{\left(\mu_X^2 + \mu_{\widehat{X}}^2 + C1\right)\left(\sigma_X^2 + \sigma_{\widehat{X}}^2 + C2\right)}, \qquad (13)$$

where μ_X, $\mu_{\widehat{X}}$, σ_X, $\sigma_{\widehat{X}}$ and $\sigma_{X\widehat{X}}$ represent the mean valve, standard deviations, and cross-covariance for images X and $\widehat{X}$, respectively. In practical applications, it is common to set the values of C1 and C2 as follows: $C1 = (0.01L)^2$ and $C2 = (0.03L)^2$, where L represents the number of gray scale levels in the image.

By analyzing these factors, we can gain a deeper understanding of the strengths and weaknesses exhibited by different algorithms. This analysis helps us identify and select the most suitable algorithms for various PAT applications. By considering factors like running time, PSNR, RE, and SSIM, we can make informed decisions regarding algorithm selection, ultimately improving the performance and effectiveness of PAT imaging techniques in specific applications.

III. EXPERIMENT AND RESULT

In this section, we evaluate six L_p-norm regularization methods, Tikhonov, L1magic, IIHT, NHTP, IHT and CGIHT, on simulated data and agar phantom data. These evaluations will provide insights into the performance of each method in terms of reconstruction accuracy, running time, and handling sparse and incomplete measurements. In the simulation experiment, the Blood vessel phantom was employed to produce signals. And in the agar phantom experiment, a homemade rotating acquisition system was used to collect photoacoustic data. The scanning radius of the rotary acquisition system was 4.5 mm, and the step size was $1.5°$. The transducer collected signals at 240 positions, and only some components were selected for sparse view image reconstruction. The sampling location number was set to 40 and 80 to obtain different sparsity. The data processing and reconstruction experiments were conducted using Matlab software on a PC with 32 GB memory and an Intel core i7-4790 processor.

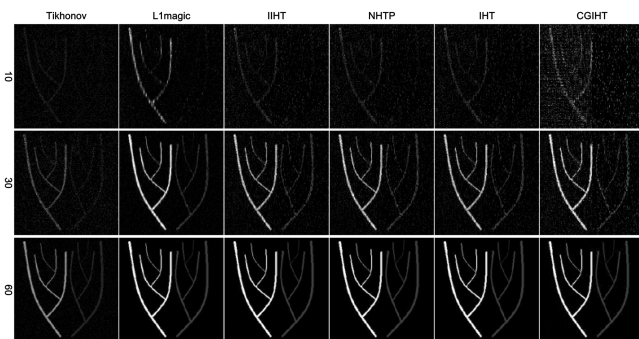Fig. 1.   Blood vessel phantom employed in simulations.

Fig. 2.   Results of the reconstruction of the blood vessel phantom. The images reconstructed by Tikhonov, L1magic, IIHT, NHTP, IHT, CGIHT methods are shown in the first to sixth columns. The results of the reconstruction of data from 10, 30, and 60 locations are shown in the first to third rows.

A. Results of Simulated Sparse-View Data

Fig. 2 presents the reconstruction results of the Blood vessel phantom using the six methods. From the analysis of these results, it is evident that the image quality in reconstructions using 10 position signals is poor and the CGIHT method introduces the highest level of noise. Furthermore, when utilizing 30 position signals for reconstruction, the L1magic method produces the clearest and most faithful image with minimal noise. Finally, when using 60 position signals for reconstruction, apart from the Tikhonov method yielding a darker image compared to the ground truth image, all the other five methods achieve satisfactory reconstruction results. For a more objective assessment of Fig. 2, please consult Fig. 3, which offers a more encompassing comparison of the six methods.

The histogram quantitative performance assessment of different algorithms based on the simulation data are shown in Fig. 3. The PSNRs, REs, and SSIMs all indicate that the three methods of IHT, IIHT, and NHTP are clearly superior to the traditional Tikhonov method. Furthermore, these three methods have similar PSNRs, REs and SSIMs, indicating comparable performance
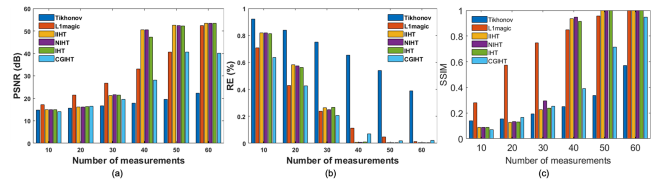

Fig. 3.   Histogram quantitative performance assessment of different algorithms based on the simulation data. (a) Histogram of PSNR. (b) Histogram of relative error. (c) Histogram of SSIM.

TABLE I
RUNNING TIME OF THE SIX TEST ALGORITHMS (S)

View Number	10	20	30	40	50	60
Tikhonov	11.29	21.85	35.26	47.02	56.1	66.86
L1magic	19.66	34.22	60.52	96.56	143.6	200.49
IIHT	10.37	485.94	136.79	68.56	23.38	83.96
NHTP	6.83	169.69	126.57	103.88	21.26	15.11
IHT	**5.45**	**13.84**	**22.13**	**28.9**	**8.16**	**3.99**
CGIHT	8.62	37.36	58.03	78.1	95.7	112.75

among them. According to the PSNR histogram presented in Fig. 3(a), the PSNR values for the three methods IHT, IIHT, and NHTP are consistently higher than those of the other three tested methods with more than 40-view measurements. This indicates that the IHT, IIHT, and NHTP methods achieve better reconstructed image quality. From the RE histogram in Fig. 3(b), it can be seen that the RE values for the three methods (IHT, IIHT, and NHTP) are consistently lower than those of the other three methods when the number of measurements exceeds 40. This suggests that the three methods exhibit better accuracy in terms of reconstruction when a larger number of measurements are used. It can be seen from Fig. 3(c) that the L1magic method produced the highest SSIM when the number of samples was less than 30. However, when the number of samples increased to 40, the IHT, IIHT, and NHTP methods achieved the best SSIM. Remarkably, when the number of samples was 60, the SSIM values for the IHT, IIHT, and NHTP methods were approximately 1, indicating excellent similarity between the reconstructed and original images.

We have compared the running time with different number of measurements. Table I shows the running times of the six methods. As can be seen in Table I, the running times of Tikhonov, L1magic and CGIHT increase with the number of measurements. This indicates that these algorithms require more computational resources and time to process a larger number of measurements. While the running time of IIHT and NHTP increases sharply and then decreases gradually. The IHT algorithm has the shortest running time among the compared algorithms, while the IIHT algorithm has the longest average running time. Additionally, when considering the PSNR, RE and running time of different algorithms in the Blood vessel phantom experiment, it suggests that the IHT algorithm is effective in reconstructing images from sparse-view data.

When an adequate number of signals are present, specifically at 50 and 60 positions, the running times of the NHTP and IHT algorithms are reduced. This improvement in running time
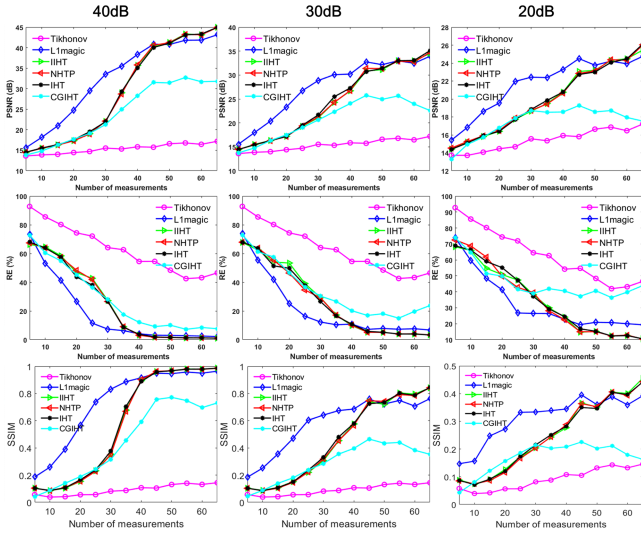
Fig. 4. Trend charts of PSNR, RE and SSIM values with increased sampling number. Columns 1–3 are the trend maps of PSNR, RE and SSIM values of reconstructed images under signals with noise of 40 dB, 30 dB and 20 dB, respectively.
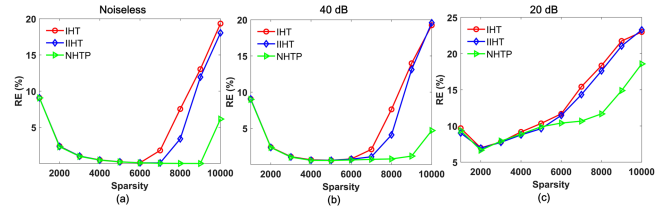

Fig. 5. Line chart of RE values of images that were reconstructed with different sparsity and 50-view simulation data. (a)–(c) are the trend maps of RE values of reconstructed images under noiseless data and signals with noise of 40 dB and 20 dB, respectively.
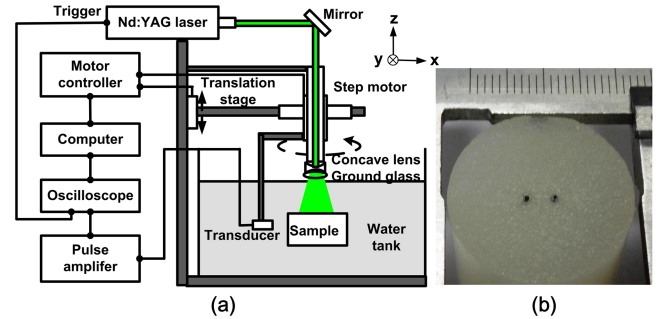

Fig. 6. (a) Structural diagram of the PAT system. (b) The photograph of the agar phantom containing two carbon rod absorbers.

can be attributed to the fact that when there are sufficient measurements, the algorithms receive more information about the underlying solution. This additional information aids in quicker convergence and reduces the number of iterations required for reconstruction. As a result, the overall computational time is shortened, making these algorithms more efficient in such scenarios.

A. Anti-Noise Ability Experiment

During the acquisition of photoacoustic signals, various types of noise are introduced, such as electronic noise, thermal noise, and shot noise. These noise sources have a detrimental impact on the quality of the acquired data, resulting in artifacts and a loss of resolution in the reconstructed image. By adding different degrees of noise to the simulated data, the influence of noise on the quality of the reconstructed image can be studied. The image reconstructed by the robust algorithm should have higher PSNR value, smaller RE value and higher SSIM value, particularly in the presence of noise.

The trend charts of PSNR, RE and SSIM values of the simulation experiment are shown in Fig. 4. Specifically, the trend of changes in PSNR and SSIM values is consistent. When the noise in the signal is 40 dB, the reconstructed images generated by the L1magic, IHT, NHTP, and IHT algorithms using more than 40 position signals exhibit PSNR values greater than 40 dB, SSIM values greater than 0.85, and RE values less than 0.1. As the noise is increased to 30 dB and 20 dB, the PSNR and SSIM values of the PAT image decrease, while the RE value increases. Overall, the L1magic method achieves the highest PSNR value and minimum RE value when the sampling location is small. When the measurement position exceeds 40, the IHT, IIHT, and NHTP algorithms yield the best experimental results. Conversely, the Tikhonov and CGIHT algorithms display the poorest reconstruction effects.

B. Parameter Tuning

In this section, we further investigated the effects of sparsity of IHT, IIHT and NHTP methods on reconstructed images based on 50-view simulation data. The sparsity values range from 1000 to 10000. Fig. 5 shows the line chart of RE values of images that were reconstructed with different sparsity. It can be seen that when the sparsity value is less than 5000, the RE values obtained by those three methods are similar. However, when the sparsity value ranges from 6000 to 10000, a difference in the RE values becomes apparent among the three methods. The IHT method has the highest RE value and the NHTP method has the lowest RE value, suggesting it performs better at higher sparsity levels. When there is no noise in the signal or the noise level is 40 dB, all three methods are capable of achieving good quantization results under the appropriate sparsity level. However, when the noise level reaches 20 dB, the RE values of all three methods are poor. This indicates that the noise has a significant influence on the IHT, IIHT and NHTP algorithms. High levels of noise can introduce artifacts, distortions, and compromise the fidelity and quality of the reconstructed images.

C. Agar Phantom Experiment

Fig. 6(a) is the PAT experiment system structure, which is similar to that of [9]. A Q-switched Nd: YAG (LS-2137U/2, Lotis TII Ltd, Belarus) laser was used as a light source to provide a laser pulse with a wavelength of 532 nm and a repetition frequency of 10 Hz. A 1 mm needle PVDF hydrophone (Precision Acoustics, U.K.) was employed to receive photoacoustic signals. The photoacoustic signals were first collected by an oscilloscope Tektronix MSO4000B and then transferred to the computer for
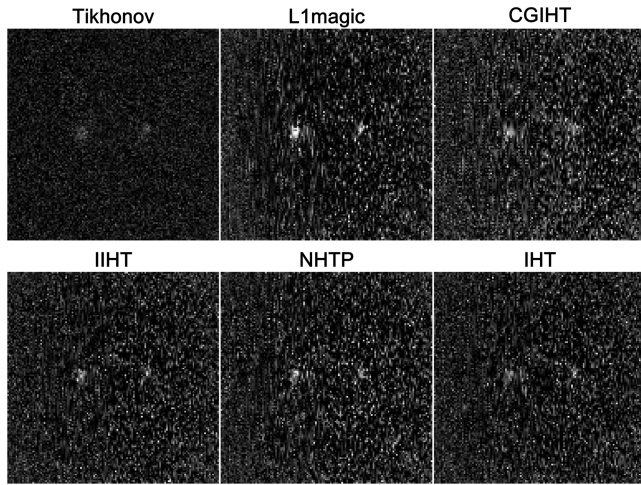
Fig. 7. Reconstructed images of the agar phantom from 40-view data using Tikhonov, L1magic, CGIHT, IIHT, NHTP and IHT, respectively.
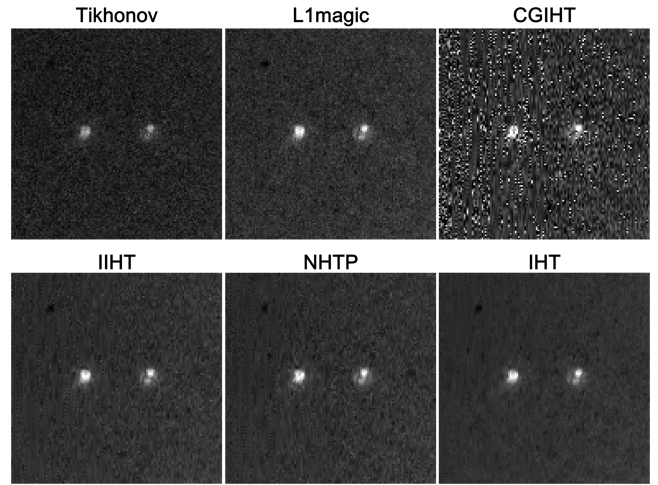

Fig. 8. Reconstructed images of the agar phantom from 80-view data utilizing Tikhonov, L1magic, CGIHT, IIHT, NHTP and IHT, respectively.
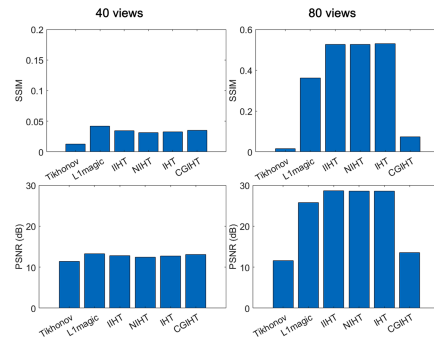

Fig. 9. Histogram quantitative performance evaluation of different algorithms based on agar phantom data. Columns 1-2 are the histograms of PSNR and SSIM values of the reconstructed image under 40-view and 80-view signals, respectively.

signal processing and PAT image reconstruction. Fig. 6(b) is the cross-sectional view of the agar phantom, in which there are two point-like carbon absorbents. In the tissue-mimicking experiment, data from 40 views and 80 views evenly distributed around the circumference were collected to reconstruct PAT images. And 64 frequency samples within the [0.15, 4.0] MHz window were randomly selected in each view.

The reconstructed images from 40-view data are shown in Fig. 7. It can be observed that serious speckle noise in all images. Only the carbon absorption samples reconstructed by the L1magic algorithm and the NHTP algorithm can see the rough outline, indicating a relatively accurate representation of the carbon absorption features. On the other hand, the carbon absorption samples reconstructed using the other four algorithms appear to be mixed with the speckle noise, resulting in a less defined representation of the carbon absorption features. This suggests that the L1magic algorithm and the NHTP algorithm may be more effective in mitigating the impact of speckle noise and preserving the structural details of the carbon absorption samples in the reconstructed images.

Fig. 8 displays the reconstructed images from 80-view data. From Fig. 8, we can see that all algorithms are capable of effectively reconstructing the carbon absorption samples in the agar phantom. However, differences can be observed in the clarity and noise level of the PAT images among the six algorithms. The image reconstructed by the IHT algorithm possesses the highest clarity. On the other hand, the image reconstructed using the CGIHT algorithm seems to be significantly affected by noise. The remaining four algorithms yield PAT images with a small amount of noise. The above experiments show that the presence of noise in the signal can have a negative impact on the quality of PAT image. Noise can introduce artifacts, distortions, and reduce the clarity of the reconstructed images. Increasing the amount of data helps to improve the signal-to-noise ratio and can result in higher-quality reconstructions.

We utilize the IHT algorithm to reconstruct the PAT image from agar phantom data with 120-view data. As the sampling angles are sufficient, the reconstructed image becomes the "standard" image for further analysis and comparison. From Fig. 9, it can be observed that the SSIM values of the reconstructed images using 40-view signals are all less than 0.05. With 80-view signals, the SSIM values of the reconstructed images are approximately 0.53 for the IHT, NHTP, and IHT algorithms, 0.36 for the L1magic method, and all less than 0.1 for the Tikhonov and CGIHT methods. The PSNR of PAT image reconstruction using IHT, NHTP, and IHT algorithms is about 28.6 dB, which is 3 dB higher than the L1magic method. It is twice as high as the Tikhonov method and CGIHT method.

IV. CONCLUSION

In this paper, six reconstruction algorithms for sparse-view PAT, Tikhonov, L1magic, IIHT, NHTP, IHT, and CGIHT, were tested and evaluated. The experimental results show that the L1magic achieves better PSNR in the case of limited data availability. By leveraging sparsity and applying L_1 regularization, the L1magic algorithm promotes a sparse representation of the reconstructed image. This sparse representation encourages the retention of important features while suppressing noise and reducing artifacts. When the signal is sparse, the reconstruction

quality of IIHT, NHTP and IHT algorithms is better than that of the traditional Tikhonov algorithm and L1magic algorithm. By iteratively thresholding and updating the coefficients of the reconstructed image, the IHT, IIHT and NHTP algorithms focus the reconstruction on the non-zero components of the sparse signal, effectively capturing and reconstructing the important features. This results in improved image quality. Additionally, the running time of the IHT method is the shortest among the six methods, while the average running time of the IIHT method is the longest.

In summary, the IHT method has better image quality, stronger anti-noise ability and minimum running time. On the other hand, the NHTP method is well-suited for scenarios with sparsity and noise due to its robustness. In our study, the sparsity parameters of the IHT, IIHT and NHTP algorithms are selected empirically. The development of adaptive techniques is an active area of research to enhance the flexibility and performance of sparse reconstruction algorithms.

REFERENCES

[1] Y. Li et al., "Snapshot photoacoustic topography through an ergodic relay for high-throughput imaging of optical absorption," *Nature Photon.*, vol. 14, no. 3, pp. 164–170, 2020, doi: 10.1038/s41566-019-0576-2.

[2] D. L. Z. Adam et al., "Carbon nanotubes as photo acoustic molecular imaging agents in living mice," *Nature Nanotechnol.*, vol. 3, no. 9, pp. 557–562, 2008, doi: 10.1038/nnano.2008.231.

[3] L. V. Wang, "Prospects of photo acoustic tomography," *Med. Phys.*, vol. 35, no. 12, pp. 5758–5767, 2008, doi: 10.1118/1.3013698.

[4] J. Lv et al., "In vivo photo acoustic imaging dynamically monitors the structural and functional changes of ischemic stroke at a very early stage," *Theranostics*, vol. 10, no. 2, pp. 816–828, 2020, doi: 10.7150/thno.38554.

[5] G. Huang, J. Lv, Y. He, J. Yang, L. Zeng, and L. Nie, "In vivo quantitative photo acoustic evaluation of the liver and kidney pathology in tyrosinemia," *Photoacoustics*, vol. 28, 2022, Art. no. 100410, doi: 10.1016/j.pacs.2022.100410.

[6] J. Zhang, L. Ning, Z. Zeng, and K. Pu, "Development of second near-infrared photoacoustic imaging agents," *Trends Chem.*, vol. 3, no. 4, pp. 305–317, 2021, doi: 10.1016/j.trechm.2021.01.002.

[7] L. Li and L. V. Wang, "Recent advances in photo acoustic tomography," *Biomed. Eng. Front.*, vol. 2, no. 2, 2021, Art. no. 9823268, doi: 10.34133/2021/9823268.

[8] T. Wang et al., "Streak artifact suppressed back projection for sparse-view photoacoustic computed tomography," *Appl. Opt.*, vol. 62, no. 15, pp. 3917–3925, 2023, doi: 10.1364/AO.487957.

[9] X. Liu et al., "Limited-view photo acoustic imaging based on an iterative adaptive weighted filtered backprojection approach," *Appl. Opt.*, vol. 52, no. 15, pp. 3477–3483, 2013, doi: :10.1364/AO.52.003477.

[10] H. Lan, J. Zhang, C. Yang, and F. Gao, "Compressed sensing for photoacoustic computed tomography using an untrained neural network," *Biomed. Opt. Exp.*, vol. 12, no. 12, pp. 7835–7848, 2021, doi: 10.1364/BOE.441901.

[11] T. Wang, M. He, K. Shen, W. Liu, and C. Tian, "Learned regularization for image reconstruction in sparse-view photo acoustic tomography," *Biomed. Opt. Exp.*, vol. 13, no. 11, pp. 5721–5737, 2022, doi: 10.1364/BOE.469460.

[12] J. Provost and F. Lesage, "The application of compressed sensing for photo-acoustic tomography," *IEEE Trans. Med. Imag.*, vol. 28, no. 4, pp. 585–594, Apr. 2009, doi: 10.1109/TMI.2008.2007825.

[13] D. Liang, H. F. Zhang, and L. Ying, "Compressed-sensing photoacoustic Imaging based on random optical illumination," *Int. J. Funct. Inform. Personalised Med.*, vol. 2, no. 4, pp. 394–406, 2009, doi: 10.1504/IJFIPM.2009.030835.

[14] X. Liu, D. Peng, W. Guo, X. Ma, X. Yang, and J. Tian, "Compressed sensing photo acoustic imaging based on fast alternating direction algorithm," *Int. J. Biomed. Imag.*, vol. 2012, 2012, Art. no. 206214, doi: 10.1155/2012/206214.

[15] S. Hakakzadeh, P. Rajendran, V. A. Nili, Z. Kavehvash, and M. Pramanik, "A spatial-domain factor for sparse-sampling circular-view photoacoustic tomography," *IEEE J. Sel. Topics Quantum Electron.*, vol. 29, no. 4, Jul./Aug. 2023, Art. no. 6800409, doi: 10.1109/JSTQE.2022.3229622.

[16] X. Li, J. Ge, S. Zhang, J. Wu, L. Qi, and W. Chen, "Multispectral interlaced sparse sampling photo acoustic tomography based on directional total variation," *Comput. Methods Prog. Biomed.*, vol. 214, 2022, Art. no. 106562, doi: 10.1016/j.cmpb.2021.106562.

[17] M. Gao, G. Si, Y. Bai, L. V. Wang, C. Liu, and J. Meng, "Graphics processing unit accelerating compressed sensing photo acoustic computed tomography with total variation," *Appl. Opt.*, vol. 59, no. 3, pp. 712–719, 2020, doi: 10.1364/AO.378466.

[18] X. Li et al., "Model-based optoacoustic tomography image reconstruction with non-local and sparsity regularizations," *IEEE Access*, vol. 7, pp. 102136–102148, 2019, doi: 10.1109/ACCESS.2019.2930650.

[19] X. Liu, S. Dai, M. Wang, and Y. Zhang, "Compressed sensing photo acoustic imaging reconstruction using elastic net approach," *Mol. Imag.*, vol. 2022, 2022, Art. no. 7877049, doi: 10.1155/2022/7877049.

[20] J. Frikel and M. Haltmeier, "Efficient regularization with wavelet sparsity constraints in photo acoustic tomography," *Inverse Problems*, vol. 34, no. 2, 2018, Art. no. 024006, doi: 10.1088/1361-6420/aaa0ac.

[21] S. Antholzer, M. Haltmeier, and J. Schwab, "Deep learning for photo acoustic tomography from sparse data," *Inverse Problems Sci. Eng.*, vol. 27, no. 7, pp. 987–1005, 2019, doi: 10.1080/17415977.2018.1518444.

[22] C. Yang, H. Lan, F. Gao, and F. Gao, "Review of deep learning for photoacoustic imaging," *Photoacoustics*, vol. 21, 2021, Art. no. 100215, doi: 10.1016/j.pacs.2020.100215.

[23] E. Anas, H. K. Zhang, J. Kang, and E. Boctor, "Enabling fast and high quality LED photo acoustic imaging: A recurrent neural networks based approach," *Biomed. Opt. Exp.*, vol. 9, no. 8, pp. 3852–3866, 2018, doi: 10.1364/BOE.9.003852.

[24] H. Lan, C. Yang, J. Cheng, J. Liu, and K. Zhou, "Ki-GAN: Knowledge infusion generative adversarial network for photoacoustic image reconstruction in vivo," in *Proc. Int. Conf. Med. Image Comput. Comput.-Assist. Interv., 22nd Int. Conf.*, 2019, pp. 273–281.

[25] C. Cai, K. Deng, C. Ma, and J. Luo, "End-to-end deep neural network for optical inversion in quantitative photo acoustic imaging," *Opt. Lett.*, vol. 43, no. 12, pp. 2752–2755, 2018, doi: 10.1364/OL.43.002752.

[26] T. Tong, W. Huang, K. Wang, Z. He, and J. Tian, "Domain transform network for photoacoustic tomography from limited- view and sparsely sampled data," *Photoacoustics*, vol. 19, 2020, Art. no. 100190, doi: 10.1016/j.pacs.2020.100190.

[27] J. Feng, J. Deng, Z. Li, Z. Sun, and K. Jia, "A comprehensive study of end-to-end UNET-based reconstruction algorithm for photo acoustic imaging," *Biomed. Opt. Exp.*, vol. 11, no. 9, pp. 5321–5340, 2020, doi: 10.1364/BOE.396598.

[28] A. Hauptmann and B. Cox, "Deep learning in photoacoustic tomography: Current approaches and future directions," *J. Biomed. Opt.*, vol. 25, no. 11, 2020, Art. no. 112903, doi: 10.1117/1.JBO.25.11.112903.

[29] X. Zhang, F. Ma, Y. Zhang, J. Wang, C. Liu, and J. Meng, "Sparse-sampling photo acoustic computed tomography: Deep learning vs. compressed sensing," *Biomed. Signal Process. Control*, vol. 71, 2022, Art. no. 103233, doi: 10.1016/j.bspc.2021.103233.

[30] M. Haltmeier, T. Berer, S. Moon, and P. Burgholzer, "Compressed sensing and sparsity in photo acoustic tomography," *J. Opt.*, vol. 18, no. 11, 2016, Art. no. 114004, doi: 10.1088/2040-8978/18/11/114004.

[31] M. Mozaffarzadeh, A. Mahloojifar, M. Nasiriavanaki, and M. Orooji, "Model-based photoacoustic image reconstruction using compressed sensing and smoothed L_0 norm," in *Proc. Photons Plus Ultrasound: Imag. Sens.*, 2018, vol. 10494, Art. no. 104943Z.

[32] X. Liu, L. Zhang, Y. Zhang, and L. Qiao, "A photoacoustic imaging algorithm based on regularized smoothed L_0 norm minimization," *Mol. Imag.*, vol. 2021, 2022, Art. no. 6689194, doi: 10.1155/2022/7877049.

[33] T. Blumensath and M. E. Davies, "Iterative hard thresholding for compressed sensing," *Appl. Comput. Harmon. Anal.*, vol. 27, no. 3, pp. 265–274, 2009, doi: 10.1016/j.acha.2009.04.002.

[34] Y. Wang et al., "Accurate and fast reconstruction for bioluminescence tomography based on adaptive Newton hard thresholding pursuit algorithm," *J. Opt. Soc. Amer. Opt. Image Sci. Vis.*, vol. 39, no. 5, pp. 829–840, 2022, doi: 10.1364/JOSAA.449917.

[35] Y. Yuan et al., "Robust transformed l(1) metric for fluorescence molecular tomography," *Comput. Methods Prog. Biomed.*, vol. 234, 2023, Art. no. 107503, doi: 10.1016/j.cmpb.2023.107503.

[36] J. Tang, A. Zhao, B. Li, and X. Song, "Fast high-quality sparse reconstruction of photo acoustic imaging based on HTP compressed sensing," *Proc. SPIE*, vol. 11815, pp. 144–148, 2021.

[37] L. Pan, S. Zhou, N. Xiu, and H. Qi, "A convergent iterative hard thresholding for nonnegative sparsity optimization," *Pacific J. Optim.*, vol. 13, no. 2, pp. 325–353, 2017.

[38] S. Zhou, N. Xiu, and H. Qi, "Global and quadratic convergence of Newton hard-thresholding pursuit," *J. Mach. Learn. Res.*, vol. 22, no. 1, pp. 599–643, 2019, doi: 10.48550/arXiv.1901.02763.

[39] J. D. Blanchard, J. Tanner, and K. Wei, "Conjugate gradient iterative hard thresholding: Observed noise stability for compressed sensing," *IEEE Trans. Signal Process.*, vol. 63, no. 2, pp. 528–537, Jan. 2015, doi: 10.1109/TSP.2014.2379665.

[40] M. Fuhry and L. Reichel, "A new Tikhonov regularization method," *Numer. Algorithms*, vol. 59, no. 3, pp. 433–445, 2012, doi: 10.1007/s11075-011-9498-x.

[41] C. B. Shaw, J. Prakash, M. Pramanik, and P. K. Yalavarthy, "Least squares QR-based decomposition provides an efficient way of computing optimal regularization parameter in photo acoustic tomography," *J. Biomed. Opt.*, vol. 18, no. 8, 2013, Art. no. 80501, doi: 10.1117/1.JBO.18.8.080501.